Supplemental Material for

Globally stable microresonator Turing pattern formation for coherent high-power THz radiation on-chip

Shu-Wei Huang[1,*,+], Jinghui Yang[1,*,+], Shang-Hua Yang[2], Mingbin Yu[3], Dim-Lee Kwong[3], T. Zelevinsky[4], Mona Jarrahi[2], and Chee Wei Wong[1,*]

[1] Fang Lu Mesoscopic Optics and Quantum Electronics Laboratory, University of California, Los Angeles, CA 90095, USA.

[2] Terahertz Electronics Laboratory, University of California, Los Angeles, CA 90095, USA.

[3] Institute of Microelectronics, A*STAR, Singapore 117865, Singapore.

[4] Department of Physics, Columbia University, New York, NY 10027, USA.

[+] These authors contribute equally.

* Author e-mail: swhuang@seas.ucla.edu ; yangjh@seas.ucla.edu ; cheewei.wong@ucla.edu

I. Spontaneous Turing pattern formation through modelled Lugiato-Lefever dynamics

In our model we numerically studied the Turing roll formation using the Lugiato-Lefever equation (LLE), $T_R \frac{\partial}{\partial t} A(t,\tau) = \sqrt{\alpha_c} A_{in} - \left[\frac{\alpha_c+\alpha_p}{2} + j\delta + j\bar{D}L + j\frac{n_2 \omega L}{c} I(t,\tau)\right] A(t,\tau)$, for its computational efficiency [S1]. Here α_p is the propagation loss, α_c is the coupling loss, δ is the detuning, and $\bar{D} = \sum_{n\geq 2} \frac{\beta_n}{n!}\left(-j\frac{\partial}{\partial \tau}\right)^n$ is the dispersion operator. The LLE was solved for 2,001 modes around the cw pump. The simulation started from vacuum noise and was run for 10^6 roundtrips until the solutions reached the steady state.

In the anomalous dispersion regime, a spontaneous growth of symmetric Turing roll was observed. As the wavelength was tuned closer to resonance, sub-comb started to emerge and destabilize the Turing pattern. The evolution dynamics with on-chip pump power of 100 mW (along the white dashed line of Figure 1a) is shown in Figure S1. On the other hand, growth of Turing roll is prohibited in the normal dispersion regime unless local dispersion disruption by mode hybridization is introduced (Figure 1c). To account for the local dispersion disruption, we artificially changed the resonance frequency of the -14th cavity mode such that $2\omega_0 - \omega_{14} - \omega_{-14}$ is phase matched. Then a spontaneous growth of Turing pattern was observed, but clearly the spectral symmetry was broken. Furthermore, sub-comb growth and transition into chaos were forbidden. The dispersion employed in the simulation is validated by both numerical modeling

and experimental measurement for microrings with different radii, as plotted in Figure S2, featuring not only a high GVD but also a large third-order dispersion. The ring radius is designed to be large enough (>160 μm) such that the bending-induced dispersion is negligible. The measured GVDs at 1603 nm (circles with error bars) show good agreements with the numerical modeling by finite-element analysis.

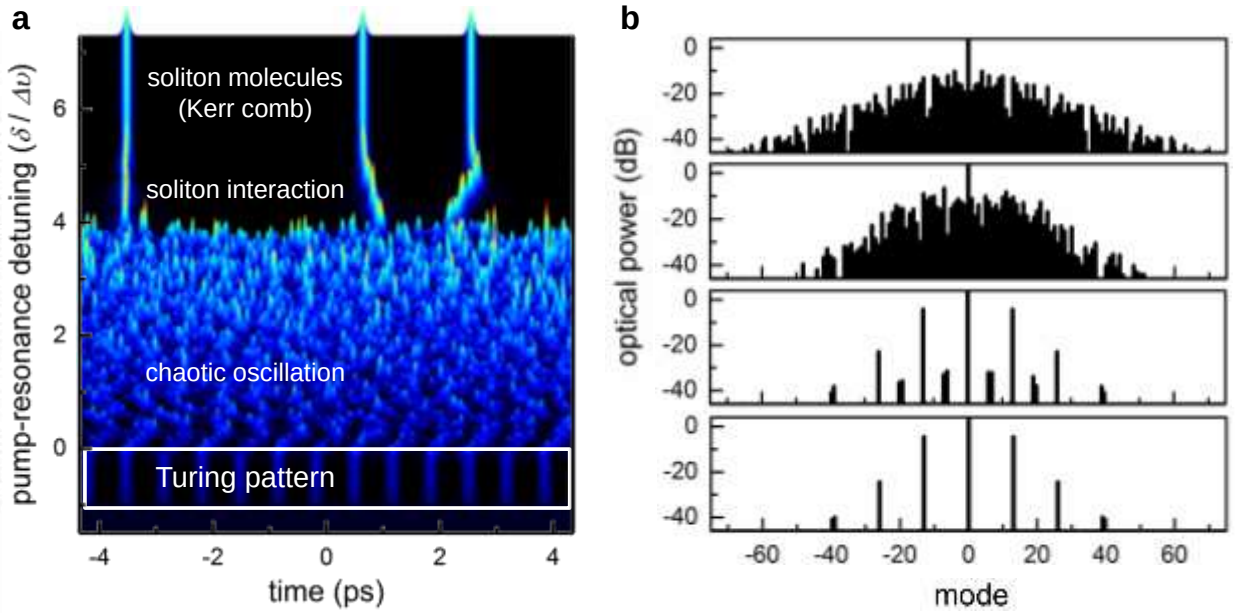

Figure S1 | Evolution dynamics in (a) temporal domain and (b) spectral domain, along the white dashed line in Figure 1a. Spontaneous Turing pattern is formed, then quickly collapsed into spatio-temporal chaos, and eventually transformed into soliton molecules with a proper scan protocol of pump detuning.

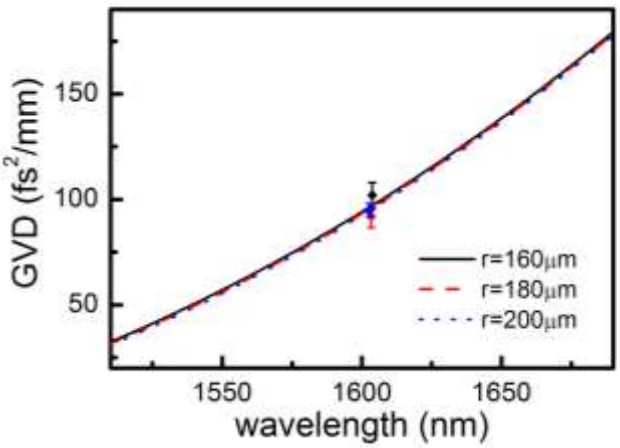

Figure S2 | Group velocity dispersion (GVD) of our ring resonators, featuring large normal GVDs of +100 fs^2/mm. The ring radius is designed to be large enough (more than 160 μm) such that the bending-induced dispersion is negligible. Measured GVDs at 1603 nm (circles with error

bars) show good agreements with the numerical modeling. Inset: scanning electron micrograph of the nonlinear ring resonator. Scale bar: 50 μm.

II. Dynamic tuning of mode hybridization by device temperature control

A series of simulated cavity resonances by 3D finite-element analysis [S6] is shown in Figure S3a. *Mode 0* is where the resonance frequencies of the two mode families (ω_{11} and ω_{12}) cross each other. The exact crossing point is determined by the distinct free spectral ranges (FSRs) of the two transverse modes (TM_{11} and TM_{21}), and it can be tuned by design of the waveguide geometry. Here without considering modal interaction effect, as Figure S3b shows, the frequency difference can be simply expressed as $\Delta_{eig}/2\pi = (\omega_{11} - \omega_{12})/2\pi$ and it has a linear relationship with the mode number.

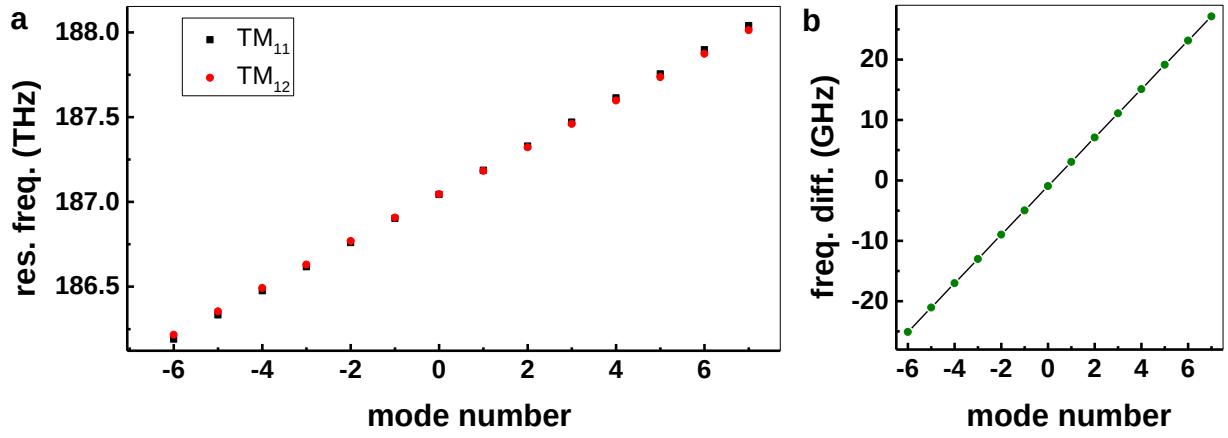

Figure S3 | Numerically modeled cavity resonances and mode crossing. (a) Resonance frequencies of TM_{11} ($\omega_{11}/2\pi$, black square) and TM_{12} ($\omega_{12}/2\pi$, red dot) at the temperature of 60 °C. (b) Frequency difference between TM_{11} and TM_{12} mode, *i.e.*, $\Delta_{eig}/2\pi$, showing a linear relationship with mode number. The crossing point between the two mode families is a function of FSR difference and can be tuned by design of the waveguide geometry.

In real devices, however, the two modes can couple with each other when their resonance frequencies are close, owing to imperfections in material growth, waveguide cross-section, and bending geometry. Figure S4a plots the experimentally measured resonance frequencies for the two modes at the temperature of 60 °C. Figure S4b shows the frequency differences calculated from the measurements at two different temperatures of 60 °C and 70 °C respectively; at *mode 0*, the cavity mode experiences a frequency shift Δ_m, leading to an offset from the otherwise linear relationship (blue lines) between the frequency difference and the mode number. Of note, Figure

S4c shows that Δ_m is inversely proportional to Δ_{eig} and their exact values are temperature dependent. Both relationships are consistent with the coupled mode theory elaborated later in details.

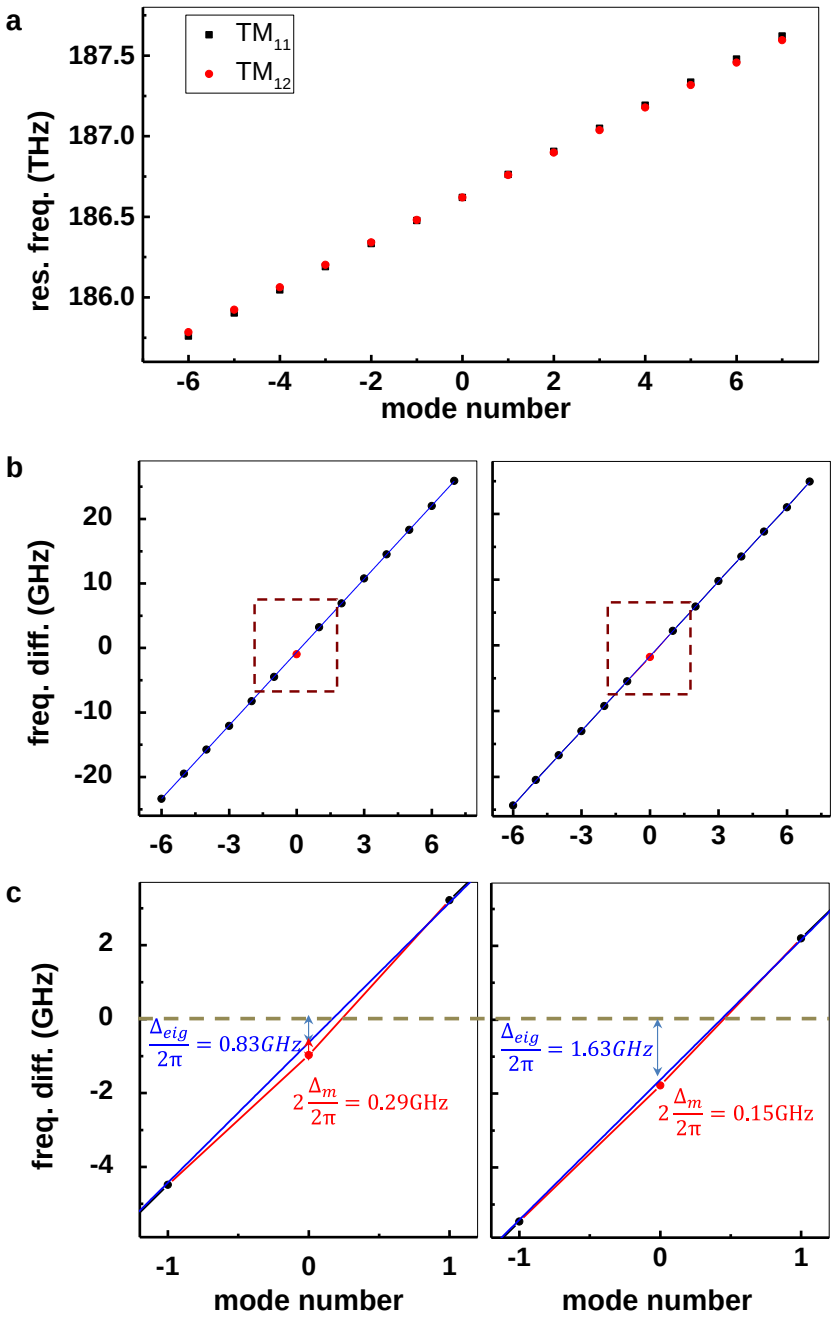

Figure S4 | (a) Experimentally measured resonance frequencies of TM_{11} (black square) and TM_{12} (red dot) at the temperature of 60 ^{o}C. (b) Frequency difference between TM_{11} and TM_{12} at 60 ^{o}C (left) and 70 ^{o}C (right). (c) Zoom-in frequency difference around *mode 0*. The linearly fitted value at *mode 0* is the frequency difference between the two

eigenmodes $\Delta_{eig}/2\pi$, 0.83 GHz at 60 ^{o}C and 1.63 GHz at 70 ^{o}C, without considering the modal interaction effect; the additional offset from the measurement (red dot) shows the modal frequency shift induced by mode hybridization $\Delta_{m}/2\pi$, 0.29 GHz at 60 ^{o}C and 0.15 GHz at 70 ^{o}C.

From the coupled mode theory, Δ_{eig} and Δ_{m} have a fixed relationship in a given device $\Delta_{m} = -\frac{\kappa^2}{\Delta_{eig}}$ [S2, S5], where κ is the mode interaction constant. Of note, while it is very challenging to control the mode interaction constant, adjusting Δ_{eig} through either waveguide design or dynamic temperature tuning is an effective way to engineer the overall effect of mode hybridization. When the magnitude of temperature tuning is sufficiently high, it can even shift the mode hybridization position, a phenomenon that is later utilized for discrete tunability of THz frequency. A summary of all measured Δ_{eig} at the temperature ranging from 30 ^{o}C to 90 ^{o}C are shown in Figure S5 (red dots). An analytic fit is performed based on the relation $R_0(1+\alpha\Delta T)n_0\left(1+\frac{\frac{1}{n_0}\frac{dn}{dT}}{\alpha}\Delta T\right)\omega = mc$ [S6], where R_0 is the original ring radius, n_0 the original index, ΔT the temperature change, m the mode number, $\frac{dn}{dT}$ the thermal optic coefficient, and α the thermal expansion coefficient [S7]. A better fit to the measurement data points (blue line) can be obtained by adjusting $\frac{dn}{dT}$ from 2.45×10^{-5} / ^{o}C as reported in the literature [S7] to 1.76×10^{-5} / $^{\circ}$C. To further validate our results, we calculate the mode interaction constant κ as a function of temperature using the measured Δ_{eig} and Δ_{m}. As expected, κ is practically temperature invariant from 50 ^{o}C to 70 ^{o}C, with a mean value of 2.1 GHz and a standard deviation of 2 % (Figure S6).

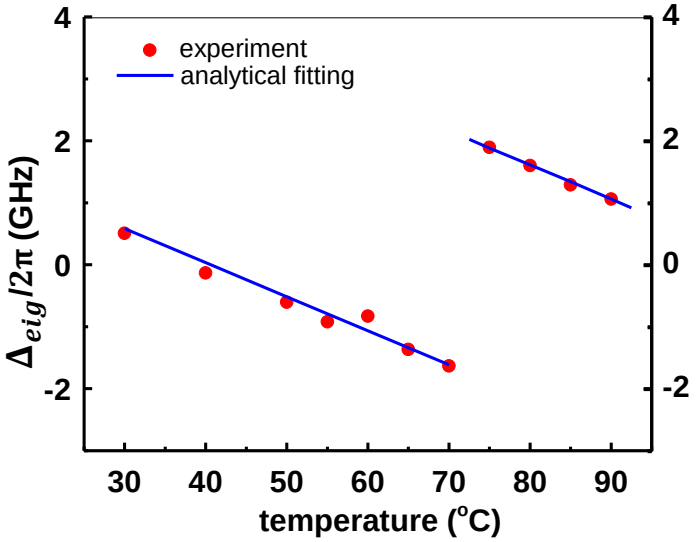

Figure S5 | Tuning of Δ_{eig} through chip temperature control, which in turn change the mode hybridization effect. Δ_{eig} shows a linear relationship with temperature. When the chip temperature is increased to more than 75 ^{o}C, the mode hybridization effect shifts to the adjacent mode.

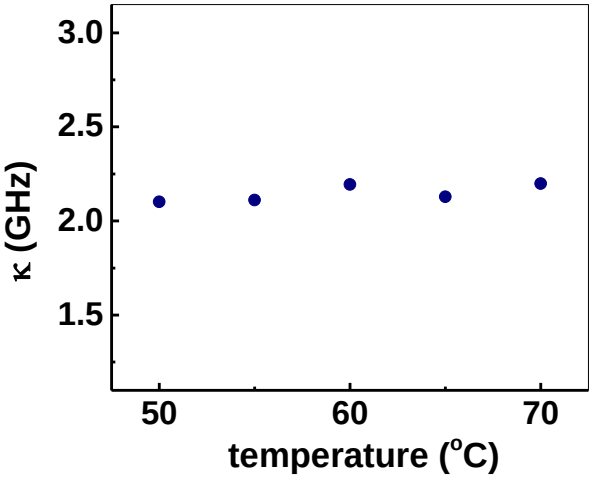

Figure S6 | Mode interaction constant κ derived from experimental measurements using the equation $\Delta_m = -\frac{\kappa^2}{\Delta_{eig}}$. Across all temperatures, the κ is consistently 2.1 GHz with 2% standard deviation.

To complete our discussion, we next quantitatively examine the mode hybridization mediated phase matching as outlined in the main text. The wavenumber with mode hybridization effect (k_1) and without mode hybridization effect (k_{1o}) can be written as:

$$k_1 = k_0 + \beta'(\Delta + \Delta_m) + \frac{\beta_2}{2}(\Delta + \Delta_m)^2$$

$$k_{1o} = k_0 + \beta'\Delta + \frac{\beta_2}{2}\Delta^2$$

hence the phase mismatch induced by mode hybridization can be expressed as $\varepsilon = k_1 - k_{1o} \approx \beta'\Delta_m + \beta_2\Delta \cdot \Delta_m$. Consequently, a modal frequency shift of $\Delta_m \approx \frac{\beta_2\Delta^2 + \gamma P_{int}}{\beta'}$ is required to satisfy the phase matching condition, $\Delta k(2\omega_0 - \omega_1 - \omega_{-1}) = \beta_2\Delta^2 + \gamma P_{int} - \varepsilon = 0$. Plugging in the measured $\Delta_m/2\pi$, $\Delta/2\pi$, β_2, β', and γ, we find the required intra-cavity power of 15 W is in a good agreement with the experiment.

III. Definition of pump-to-comb power conversion efficiency

As shown in Figure S7, here the pump-to-comb power conversion efficiency is defined as:

$$\eta = \frac{\int_0^T (I_{out} - I_{bkg})dt}{T}$$

In the calculation, we only consider the optical power of the Turing pattern carried by the output bus waveguide. This definition of power conversion efficiency, rather than slope efficiency or internal efficiency, is adopted in this manuscript because it provides a more transparent measure to calculate the total available power for real-world applications.

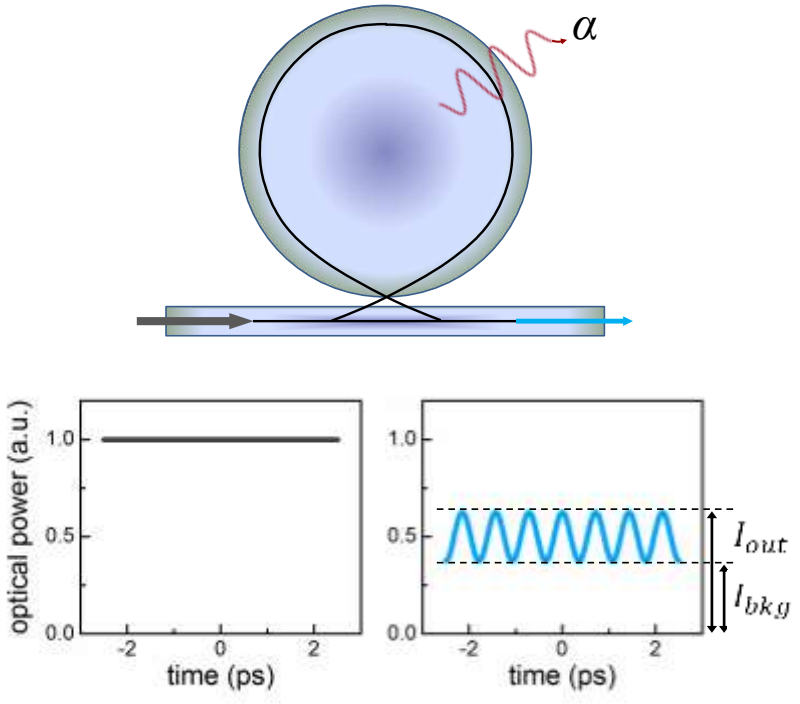

Figure S7 | Illustration of external pump-to-comb conversion efficiency.

IV. Turing rolls for coherent high-power tunable THz generation

Figure S8 shows the intensity autocorrelation (IAC) profile of the Turing roll at the stage III. Due to the efficient energy conversion from the pump to the first sideband pair, the Turing roll features a quasi-sinusoidal intensity profile with a negligible background of less than 1% of the peak intensity. Nearly background-free operation is important for efficient on-chip THz generation as it reduces the risk of thermal breakdown at high optical pump powers.

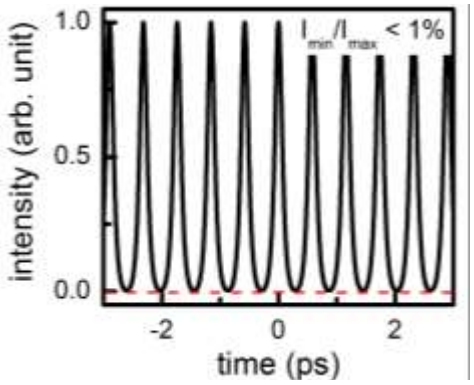

Figure S8 | Measured intensity profile of the sub-picosecond Turing roll, showing a quasi-sinusoidal oscillation with a more than 100 contrast.

V. Temporal dynamics of the Turing pattern formation

To probe the robustness of the Turing pattern formation to the perturbations in initial conditions and pump wavelength tuning speeds, we recorded IAC traces of the Turing rolls generated under three different tuning speeds on two different days. The results are summarized in Figure S9. Unlike the microresonator soliton generation where the initial condition and the tuning speed play key roles in determination of the soliton states, here the Turing roll always evolves in the identical route and is robust against perturbations in initial conditions and pump wavelength tuning speeds.

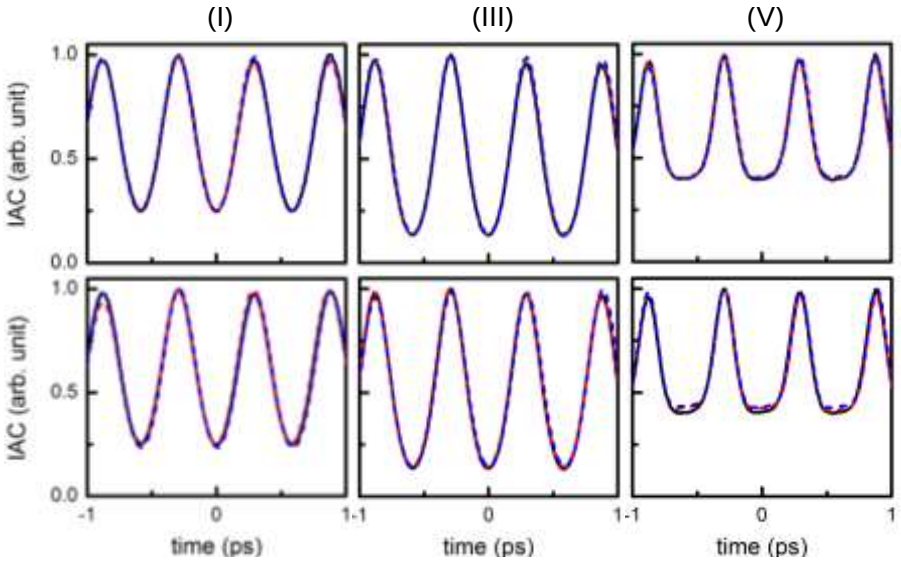

Figure S9 | At three different scanning speeds (black curve: 1 nm/s; red dashed curve: 0.3 nm/s; blue dashed curve: 0.1 nm/s) and two independent starts (top and bottom), the Turing roll shows the identical generation route.

Figure S10 illustrates how applying an additional dispersion (30 cm SMF28) leads to different temporal structure changes of the Turing pattern at two example detunings. The effect can be understood as the consequence of the pump phase slip around the resonance. As shown in Figure S11a, the output pump will experience a π phase shift as it traverses through the resonance. Such phase slip is due to the interference between the intracavity and the input pump and thus the other sidebands of the Turing roll will not experience such a phase shift. This additional pump phase slip results in the observed change of temporal structure. The distinct responses to dispersion illustrated in Figure S10 are well captured by considering the pump phase offset (Figure S11). Of note, most of the phase slip happens very close to cavity resonance and thus the observation of its effect is attributed to the unique design of our microresonator, where the effect of mode hybridization mediated phase matching of spontaneous Turing pattern formation prevents the Turing pattern destabilization even when the pump is deep into the resonance.

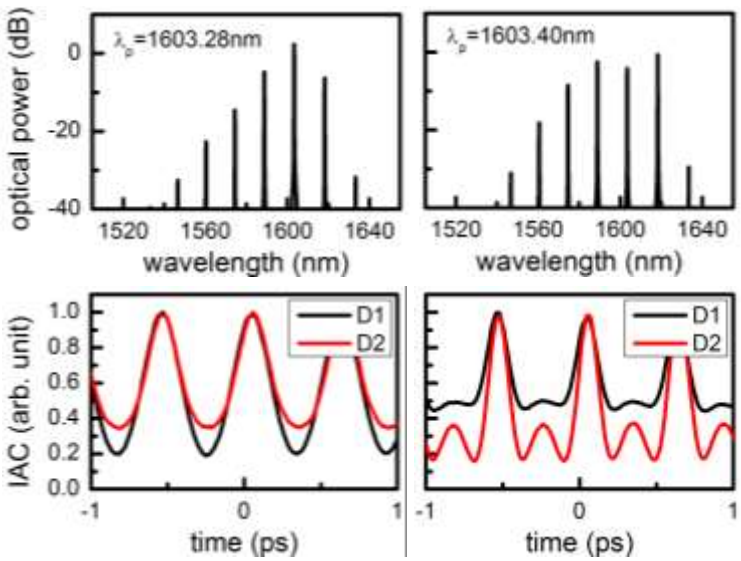

Figure S10 | IAC traces of the Turing rolls at two different pump detunings (λ_p = 1603.28 nm and λ_p = 1603.40 nm) with two external dispersion compensation. Here D1 and D2 use 60 cm and 90 cm SMF-28 fibers as the external dispersion elements, respectively.

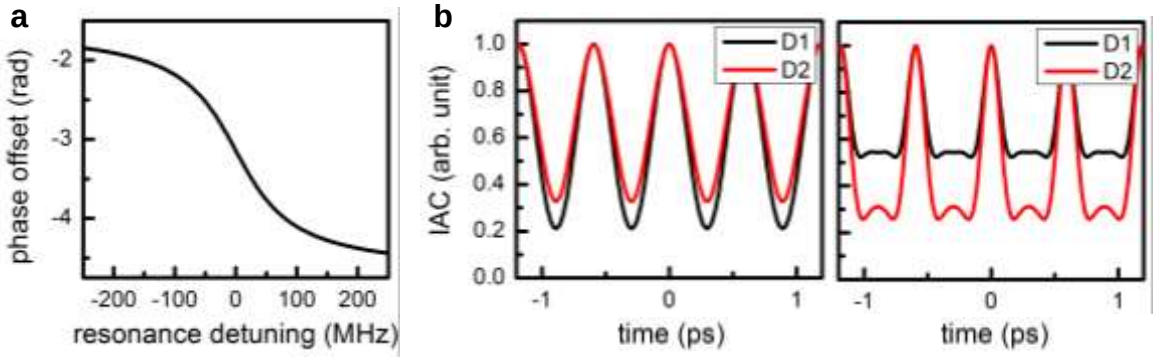

Figure S11 | (**a**) Phase offset between the intracavity and output pump light, showing a π phase slip around the resonance. (**b**) IAC traces calculated by adding π/2 to the pump wavelength for λ_p = 1603.40 nm, showing a good agreement with the measurements shown in Figure S10.

VI. Microresonator characterizations and Turing pattern measurements

Figure S12 shows the schematic diagram of the dispersion measurement setup [S5]. The microresonator transmission was recorded when the laser was swept from 1550 nm to 1630 nm at a tuning speed of 40 nm/s. The sampling clock of the data acquisition is derived from the photodetector monitoring the laser transmission through a fiber Mach-Zehnder interferometer with 40 m unbalanced path lengths, which translates to a 5 MHz optical frequency sampling resolution. Transmission of the hydrogen cyanide gas cell was simultaneously measured and the absorption features were used for absolute wavelength calibrations. Each resonance was fitted

with a Lorentzian lineshape to determine the resonance frequency and the quality factor. The microresonator dispersion was then calculated by analyzing the wavelength dependence of the free spectral range.

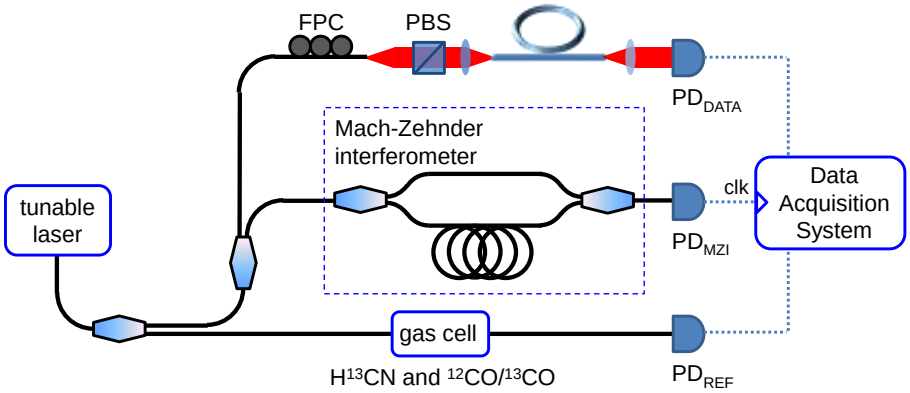

Figure S12 | Microresonator dispersion measurement setup.

To probe the equidistance of the Turing roll sidebands, a uniformity measurement setup is employed as shown in Figure S13. The generated Turing roll was split and sent to 3 beat detection units (BDUs) individually optimized for the wavelength of the pump (1603 nm), the 1st sideband (1589 nm), and the 2nd sideband (1575 nm). Heterodyne beat notes were generated between the Turing roll (green arrows) and a reference fiber laser frequency comb (red arrows). The gratings in the BDUs critically suppress the unwanted reference fiber laser frequency comb teeth such that clean heterodyne beat notes with more than 40 dB signal to noise ratio (measured with a 100 kHz resolution bandwidth), sufficient for reliable measurements, can be routinely obtained. The beat notes from the sidebands (δ_1 and δ_2) were mixed with the beat note from the pump (δ_0) to cancel the residual pump wavelength instability before being measured by a high-resolution frequency counter (10 mHz frequency error at 1 second). The frequency counter was operated in the ratio counting mode, to circumvent the synchronization challenge of simultaneous beat note measurements and achieve a more accurate measurement.

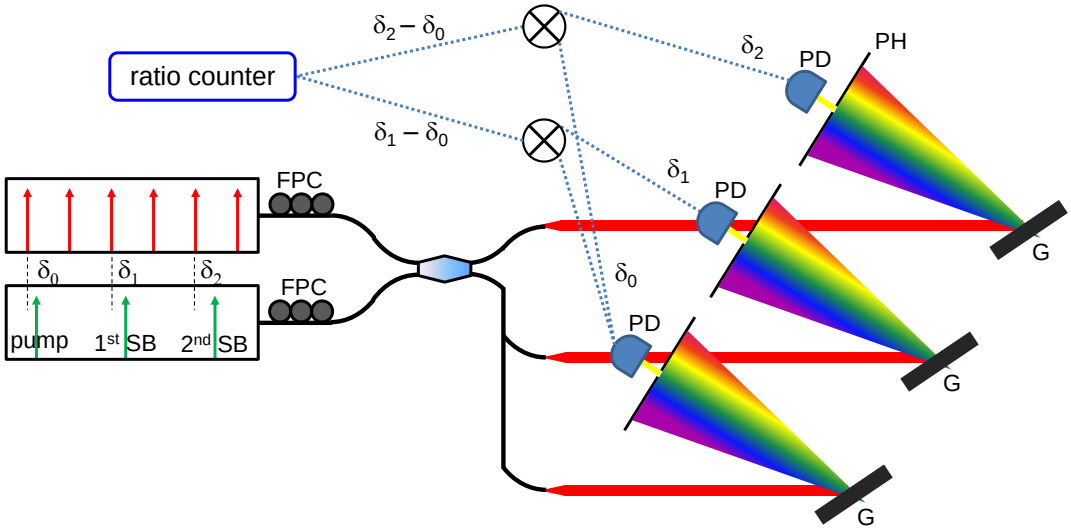

Figure S13 | Turing pattern sideband frequency uniformity measurement setup.

Figure S14 shows the schematic diagram of the self-heterodyne linewidth measurement setup [S8]. The input was split into two parts with 70% of it being sent through an acousto-optic modulator which shifts the optical frequencies by 200 MHz. The other portion was sent through a 5 km single mode optical fiber, providing a time delay of 24.5 μs. Both lights were then recombined, and the resulting beat note was recorded and analyzed with a high-speed photodetector and an electrical spectrum analyzer. The RF spectrum becomes a self-convolution of the laser spectrum, from which the linewidth can be retrieved, as long as the coherence length is shorter than the introduced delay. Thus our self-heterodyne measurement setup can measure a minimum linewidth at 13 kHz, about 40 times smaller than the measured laser linewidth.

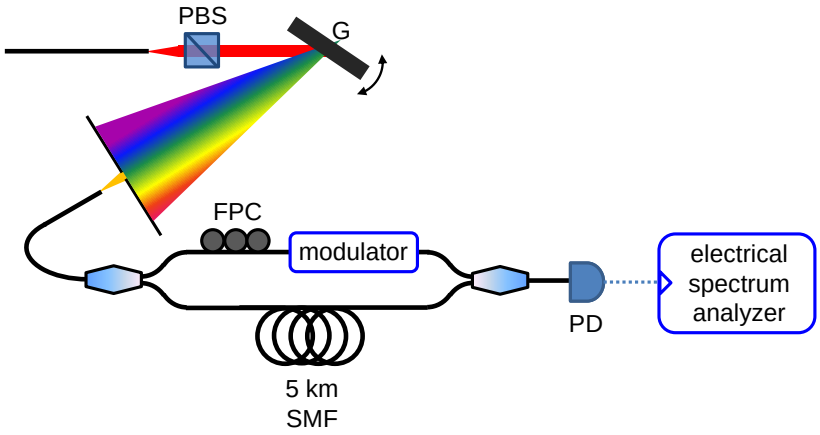

Figure S14 | Self-heterodyne measurement setup.

Figure S15 shows the schematic diagram of the linewidth and drift of the THz carrier measurement setup. The pump and one of the sideband are beat with the adjacent fiber laser frequency comb lines, and two beat signals are electrically mixed to get the beat note of the frequency difference.

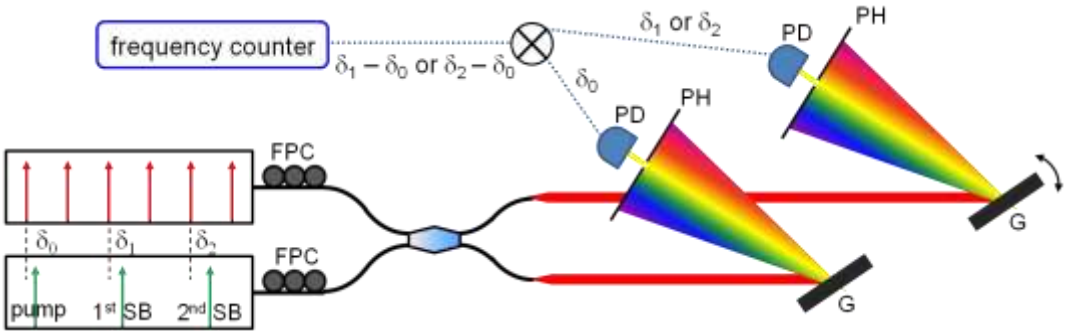

Figure S15 | Turing pattern frequency stability characterization setup.

Figure S16 shows the schematic diagram for THz frequency stabilization setup. The first Turing sideband is filtered out and sent to a photodetector to monitor the power fluctuation. A computer program is used as the loop filter that takes in the Turing sideband power fluctuation as the error signal and outputs the control signal to modulate the pump power. The computer-aided slow feedback loop has a bandwidth of 1 Hz.

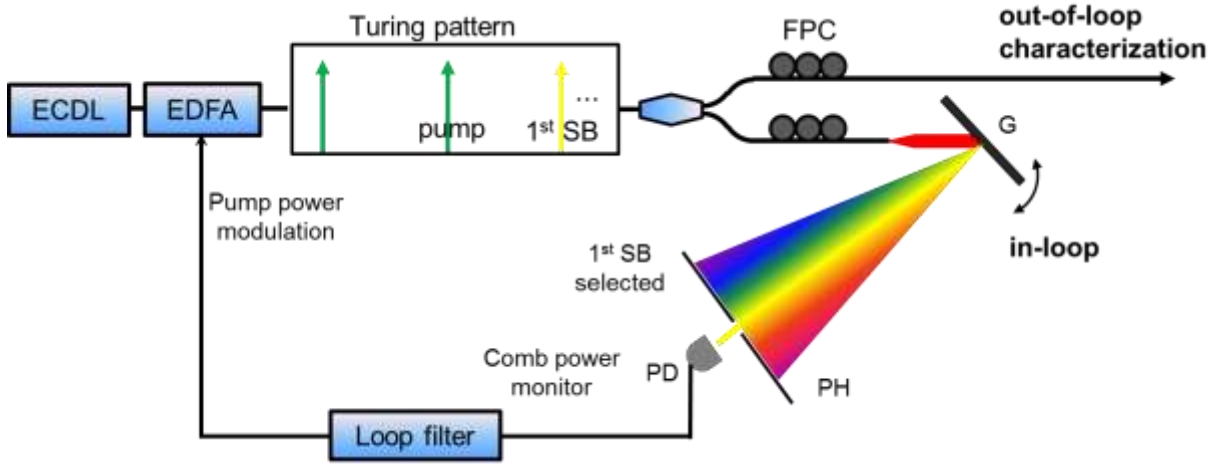

Figure S16 | Turing pattern frequency stabilization setup.

Figure S17 shows the schematic diagram of the THz radiation generation setup. A C/L WDM filter, followed by an erbium doped fiber amplifier (EDFA), was used to selectively amplify the Turing roll sidebands in the 1530 to 1565 nm C-band range. A 500 kHz intensity modulator was utilized to reduce the duty cycle of the Turing roll to 1%, thereby increasing the

thermal breakdown onset threshold. Efficient photomixing [S3] is achieved based on a logarithmic spiral plasmonic antenna design [S4] for efficient THz radiation generation. To achieve the highest photomixing efficiency, both the focus spot size and the position of the optical pump were adjusted to maximize the induced photocurrent level. The generated THz radiation was then measured with a liquid helium-cooled silicon bolometer. Lock-in detection technique was implemented to reduce the noise level and obtain a more reliable reading of the THz radiation power.

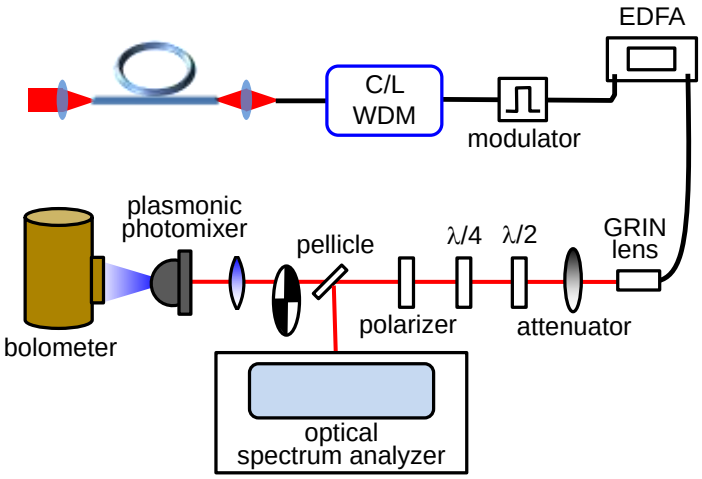

Figure S17 | THz radiation generation setup.

Supplemental References:

[S1] S. Coen, H. G. Randle, T. Sylvestre, and M. Erkintalo, "Modeling of octave-spanning Kerr frequency combs using a generalized mean-field Lugiato–Lefever model," *Opt. Lett.* **38**, 37 (2013).

[S2] A. A. Savchenkov, A. B. Matsko, W. Liang, V. S. Ilchenko, D. Seidel, and L. Maleki, "Kerr frequency comb generation in overmoded resonators," *Opt. Express* **20**, 27290 (2012).

[S3] H. Tanoto, J. H. Teng, Q. Y. Wu, M. Sun, Z. N. Chen, S. A. Maier, B. Wang, C. C. Chum, G. Y. Si, A. J. Danner, and S. J. Chua, "Nano-antenna in a photoconductive photomixer for highly efficient continuous wave terahertz emission," *Sci. Rep.* **3**, 2824 (2013).

[S4] C. W. Berry, M. R. Hashemi, S. Preu, H. Lu, A. C. Gossard, and M. Jarrahi, "High power terahertz generation using 1550 nm plasmonic photomixers," *Appl. Phys. Lett.* **105**, 011121 (2014).

[S5] S.-W. Huang, H. Zhou, J. Yang, J. F. McMillan, A. Matsko, M. Yu, D.-L. Kwong, L. Maleki, and C. W. Wong, "Mode-locked ultrashort pulse generation from on-chip normal dispersion microresonators," *Phys. Rev. Lett.* **114**, 053901 (2015).

[S6] L. Zhang, Y. Yue, R. G. Beausoleil, and A. E. Willner, "Analysis and engineering of chromatic dispersion in silicon waveguide bends and ring resonators," *Opt. Express* **19**, 8102 (2011).

[S7] A. Arbabi and L. L. Goddard, "Measurements of the refractive indices and thermo-optic coefficients of Si_3N_4 and SiOx using microring resonances," *Opt. Lett.* **38**, 3878 (2013).

[S8] T. Okoshi, K. Kikuchi, and A. Nakayama, "Novel method for high resolution measurement of laser output spectrum," *Electron. Lett.* **16**, 630 (1980).